Quantum fluctuations in very small laser diodes

Kaushik Roy-Choudhury

Department of Physics and Astronomy, University of Southern California, Los Angeles, California 90089-0484, USA

A. F. J. Levi

Department of Physics and Astronomy, University of Southern California, Los Angeles, California 90089-0484, USA, and
Department of Electrical Engineering, University of Southern California, Los Angeles, California 90089-2533, USA

Quantum fluctuations play a critical role in determining the steady-state and transient response of a laser when there is a small number of particles in the system. These fluctuations, and the fact that a lowest energy state of the system exists, can suppress lasing and enhance spontaneous emission around threshold. Dynamic switching between two characteristic system states can dominate the fluctuations. Correlations between n discrete excited electronic states and s discrete photons create a non-Poisson probability distribution and damp the average dynamic response of laser emission.

I. INTRODUCTION

Laser diodes are employed in diverse and important applications. They are used in fiber-optic communication systems for the Internet, they are essential for all optical storage, and they enable high-quality, low-cost printing. Understanding how laser diodes work, in particular how they might be reduced in size, is of interest because small devices might cost less and thereby find new uses. Unlike standard laser diodes, we will show that small lasers can behave differently and are, in fact, an example of a finite-sized quantum system in which correlated particle number fluctuations dominate behavior.

The physics determining operation of a conventional laser is quite well understood in the thermodynamic limit. In this case there is a large number of excited states in the system, the fraction of spontaneous emission, β, feeding into the lasing optical mode is small ($\beta \sim 10^{-4}$), and there is a well-defined threshold between incoherent nonlasing photon emission and coherent lasing photon emission. The approximate behavior of these systems may be described using continuum mean-field rate equations. Beyond these relatively crude models, quantum statistical theories of laser operation exist. When evaluated in the large particle number limit, they successfully reproduce the continuum mean-field results and may be used to model particle number fluctuations and statistics in the thermodynamic limit. Well-established models of this type include Fokker-Plank equations developed by Haken [1] and a density matrix approach by Scully and Lamb [2–4]. The ensemble averages used in these models cannot be applied to small systems involving a few particles. However, they do highlight the importance of quantum fluctuations in relatively large lasers. For example, experiments show that fluctuations in photon number play an essential role in determining the temperature dependence of conventional laser diodes [5–7]. In these devices, and in agreement with the Landau-Ginzburg theory of phase transitions, fluctuations enhance photon emission below threshold and suppress spontaneous emission. This behavior occurs because the devices are large and operate in the thermodynamic limit. The situation is expected to be qualitatively different when the laser is small and the discrete quantum nature of the particles in the system influences

device behavior. It is this change in the physics determining laser operation that we set out to address.

Recently, a considerable amount of research has focused on developing small lasers with ultralow threshold values [8–11]. One idea employs the cavity-quantum electrodynamics (QED) effect [12] in which optical emission from an atom may be modified by changing its electromagnetic environment. The threshold of single-mode lasers can be reduced if the fraction of spontaneous emission, β, feeding into the lasing mode is increased. This is achieved by inhibiting emission into nonlasing optical modes using high-quality-factor (high-Q) microcavities. The limiting case is $\beta = 1$ in which all the spontaneous emission feeds into the lasing mode.

Typically, continuum mean-field rate equations have been employed to describe laser diode behavior. The equations used are of the form

$$\frac{d\langle n\rangle}{dt} = -B\langle n\rangle^2 - \frac{a\Gamma c}{V n_{\mathrm{r}}}\langle (n-n_0)\rangle\langle s\rangle + \frac{I}{e}, \qquad (1)$$

$$\frac{d\langle s\rangle}{dt} = \beta B\langle n\rangle^2 + \frac{a\Gamma c}{V n_{\mathrm{r}}}\langle (n-n_0)\rangle\langle s\rangle - \kappa\langle s\rangle, \qquad (2)$$

where $\langle n\rangle$ is the mean carrier number in the active volume V and $\langle s\rangle$ is the mean photon number in the optical cavity. In the equations, $\frac{a\Gamma c}{V n_{\mathrm{r}}}\langle (n-n_0)\rangle\langle s\rangle$ is the stimulated emission term for a bulk active region, c is the speed of light in vacuum, n_0 is the carrier number at optical transparency, a is the optical gain slope coefficient, Γ is the optical confinement factor, and n_{r} is the refractive index of the medium. The term $-B\langle n\rangle^2$ describes spontaneous emission, where $B = B'/V$ and B' is the spontaneous emission coefficient. Other contributions to the carrier recombination are often included in (1). For example, $-A_{\mathrm{nr}}\langle n\rangle$ can be used to describe nonradiative recombination and $-(C/V^2)\langle n\rangle^3$ is a nonlinear contribution to recombination. The term $\kappa\langle s\rangle$ denotes cavity loss of photons, where $\kappa = \frac{c}{n_{\mathrm{r}}}[\alpha_i + \frac{1}{2L_{\mathrm{c}}}\ln(\frac{1}{r_1 r_2})]$, cavity length is L_{c}, mirror reflectivity is $r_1 = r_2 = r$, and α_i is the internal optical loss. The injection current is I and e is the electron charge. As shown in Fig. 1 calculations using (1) and (2) predict the threshold behavior in mean photon number $\langle s\rangle$ with injection current I smoothes with increasing β and disappears entirely for $\beta = 1$.
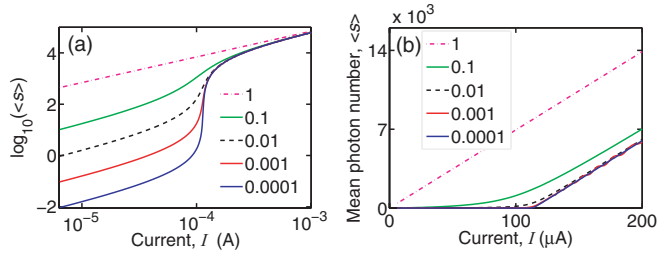
FIG. 1. (Color online) Continuum mean-field rate-equation calculation of mean photon number, $\langle s \rangle$, as a function of injection current, I, for the indicated values of β showing transition to "thresholdless" lasing in the limit $\beta = 1$. (a) $\log_{10}\langle s \rangle$ as a function of $\log_{10} I$. (b) $\langle s \rangle$ as a function of I. Parameters: $V = (5 \times 1 \times 1 \ \mu\text{m})$, $\Gamma = 0.25$, $a = 2.5 \times 10^{-16} \ \text{cm}^2 \ \text{s}^{-1}$, $B' = 10^{-10} \ \text{cm}^3 \ \text{s}^{-1}$, $n_0 = 10^{18} \ \text{cm}^{-3}$, $\alpha_i = 10 \ \text{cm}^{-1}$, $n_r = 4$, $r = 0.999$.

Figure 2 shows images of semiconductor lasers where continuum mean-field rate equations can be applied. Figure 2(a) is a photograph of a conventional Fabry-Perot laser diode. Cavity length is $L_c = 300 \ \mu\text{m}$, $\beta = 5 \times 10^{-5}$, and the active volume is 15 μm^3. The horizontal metal stripe makes contact with a p-type semiconductor, the substrate is n-type, and six quantum wells form the active volume at the diode p-n junction. The device parameters are that of an $\text{In}_{0.7}\text{Ga}_{0.3}\text{As}_{0.6}\text{P}_{0.4}$ laser with emission at 1310 nm wavelength [13]. Figure 2(b) shows a microdisk laser [14] which has an active volume approximately 100 times smaller compared to that of the Fabry-Perot laser. The much larger value of $\beta = 10^{-1}$ for this device is achieved by reducing optical cavity size.

The continuum mean-field rate equations, useful for large and intermediate-sized systems, is an approximate calculation of the first moment in the distribution of n and s. A description using only the first moment $\langle n \rangle$ and $\langle s \rangle$ is not sufficient to describe the behavior of lasers scaled to have small active volumes. Any model of very small lasers should explicitly include fluctuations and be able to calculate higher-order moments in the distribution of n and s.
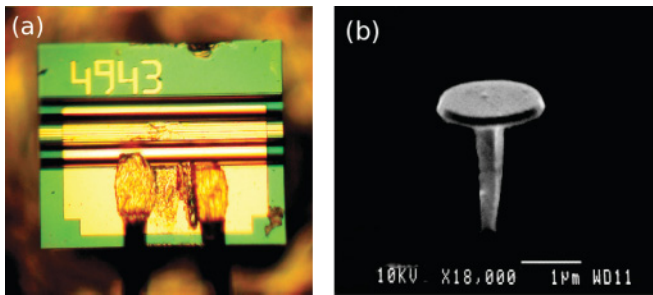

FIG. 2. (Color online) (a) Photograph from the top surface of a typical Fabry-Perot laser diode with $L_c = 300 \ \mu\text{m}$ and $I_{\text{th}} = 3$ mA. Photon cavity round-trip time in the device is 8 ps. The horizontal metal stripe makes electrical contact with a p-type semiconductor. Gold wire bonds connect to the anode of the current supply, driving the laser. The n-type semiconductor contact is made via the backside of the semiconductor substrate. (b) Scanning electron microscope image of an optically pumped microdisk laser. Image from [14]. Disk diameter is 1.6 μm and the photon cavity round-trip time is 0.06 ps.

In principle, a quantum theory of laser operation can incorporate these higher-order effects. However, the approximations typically employed constrain them to either large-scale systems or single atoms. The problem of a single two-level atom in an optical cavity is solvable and has been extensively studied in quantum optics [1,4,15,16]. In fact, theoretical predictions for light emission from single atoms and single quantum dots [17–19] in optical microcavities exhibit interesting features such as self-quenching and squeezed light emission. Extension of this approach to include multiatom effects requires numerical computation. Unfortunately, the number of system states scales as $(2^n)s$, where n is the number of two-level atoms present and s is the number of cavity photons. Thus, the problem becomes computationally challenging with increasing number of atoms inside the cavity because the coefficient matrix is of order $(4^n)s \times (4^n)s$. Cases studied so far involve 1 or 2 atoms and solutions are obtained numerically by truncating the coupled density matrix equations [19]. Treatments involving arbitrary numbers of excited states include approximations of a reservoir level, which excludes interesting phenomena appearing in the small-scale limit [20]. Systematic studies have also been performed for micromasers where bulk and single particle effects (trapped states) have been investigated [21] but the maximum number of atoms simultaneously present in the cavity was limited to 5. By modifying the injection technique [22], up to 100 atoms have been included in the cavity.

Here, we develop a description that quantizes particle energy and allows study of meso-scale systems. Our approach captures the most significant quantum effects in these small-scale systems. In particular, it allows exploration of quantum fluctuations and its impact on the behavior of small laser diodes.

This article is organized as follows. In Sec. II we explore the behavior of small lasers using a technique based on a random walk method. Description of the method is followed by calculation of the steady-state characteristics of meso-scale devices. Convergence with continuum mean-field rate-equation results is achieved for large systems. Sec. III discusses the use of master equations to study similar systems. This approach gives predictions in agreement with those of Sec. II. Section IV applies the methods of Secs. II and III to the study of transient characteristics. Section V addresses aspects of experimental design and Sec. VI is a summary and describes possible future directions.

II. RANDOM WALK TRAJECTORY

To capture the physics dominating the meso-scale behavior of laser diode operation when there is only a small number of excited states in the system, we have used a technique based on a biased random walk or Monte-Carlo trajectory [23]. Quantization of n discrete excited electronic states and s discrete photons is achieved by assuming the system may be described by the state (n, s).

Consider the system at time $t = 0$ containing n excited two-level electronic states, each separated in energy by $\hbar\omega$ and s photons, each of energy $\hbar\omega$. Figure 3 illustrates the transitions in and out of state (n, s). The term $-\beta B n^2$ describes the spontaneous emission of photons involving
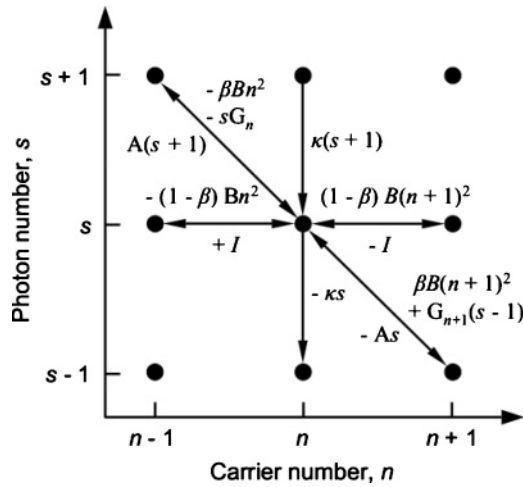
FIG. 3. Transition rates in and out of quantum state (n, s). Positive signs indicate flow into the state and negative signs flow out of the state. B is the spontaneous emission coefficient, $-G_n s = (a\Gamma cn/Vn_r)s$ is the stimulated emission rate in the system at photon energy $\hbar\omega$, $-As = (a\Gamma cn_0/Vn_r)s$ is the stimulated absorption rate, n_0 is the transparency carrier number, c is the speed of light in vacuum, Γ is the overlap of the optical field intensity with the gain medium, a is the gain slope coefficient, and n_r is the refractive index of the active volume V. The total optical loss rate from the Fabry-Perot cavity is $\kappa s = \frac{c}{n_r}[\alpha_i + \frac{1}{2L_c}\ln(\frac{1}{r_1 r_2})]s$, where $r_1 = r_2$ is the mirror reflectivity, α_i is the internal loss, and L_c is the cavity length. I is the injection (pump) current and e is the electron charge.

transitions from state (n, s) to state $(n - 1, s + 1)$, where $B = B'/V$ and B' is the spontaneous emission coefficient. $-sG_n$ describes stimulated emission of photons from state (n, s) to state $(n - 1, s + 1)$, where G_n is the stimulated emission coefficient. $-(1 - \beta)Bn^2$ is the decay of electrons into nonlasing photons via transitions from state (n, s) to state $(n - 1, s)$. Current $+I$ denotes injection of electrons causing transitions from state (n, s) to state $(n + 1, s)$. $-As$ is stimulated absorption of photons involving transitions from state (n, s) to state $(n + 1, s - 1)$, where A is the stimulated absorption coefficient. $-\kappa s$ describes the decay of cavity photons in which transitions from state (n, s) to state $(n, s - 1)$ occur, where κ is the optical loss coefficient.

The system evolves by transitioning between neighboring states via the processes indicated in Fig. 3. The time constants, τ_i, of all possible independent transitions involving the state (n, s) are calculated. The next time step is calculated using $t_i = -\tau_i \ln(\text{RAND})$ where the subscript labels the channel and RAND is a uniformly distributed random number between zero and one. The channel with the lowest t_i is chosen and the system makes a move to the new state in time t_i. The process involves a series of biased random transitions on a grid whose trajectories sample the continuous probability function $P_{n,s}$ for each state (n, s). Steady-state probability distribution for a particular injection current is obtained by averaging over multiple trajectories, where each trajectory consists of millions of time steps. The probability of state (n, s) is $P_{n,s}$. This probability is estimated from the relative time spent in state (n, s).

Fluctuations and correlations are expected to have a strong effect on the behavior of small lasers. Figure 4 shows steady-
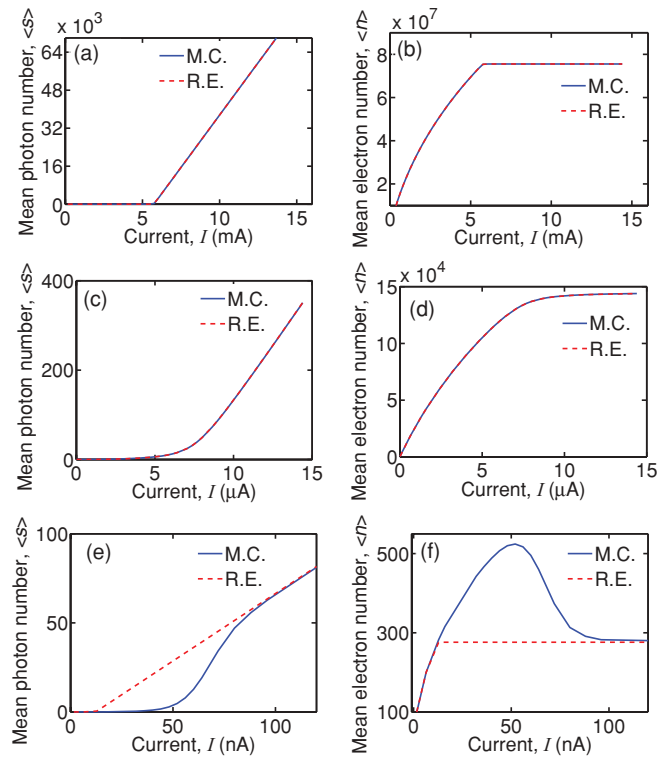

FIG. 4. (Color online) Steady-state characteristics. Mean photon and electron number in the device plotted as a function of injection current. Continuum mean-field rate-equation calculation (dashed line, R.E.) compared with results from our random trajectory Monte-Carlo technique (solid line, M.C.). (a, b) Fabry-Perot laser, (c, d) microdisk laser, (e, f) laser with meso-scale active volume. Parameters for (a) and (b): $V = (300 \times 0.8 \times 0.14 \ \mu\text{m})$, $\Gamma = 0.25$, $a = 2.5 \times 10^{-16} \ \text{cm}^2 \ \text{s}^{-1}$, $B' = 10^{-10} \ \text{cm}^3 \ \text{s}^{-1}$, $A_{nr} = 2 \times 10^8 \ \text{s}^{-1}$, $C = 10^{-29} \ \text{cm}^6 \ \text{s}^{-1}$, $n_0 = 10^{18} \ \text{cm}^{-3}$, $\alpha_i = 40 \ \text{cm}^{-1}$, $n_r = 3.3$, $r = 0.32$, $\beta = 5 \times 10^{-5}$. Parameters for (c) and (d): $V = [\pi \times (0.8 \ \mu\text{m})^2 \times 0.06 \ \mu\text{m}]$, $\Gamma = 0.25$, $a = 2.5 \times 10^{-16} \ \text{cm}^2 \ \text{s}^{-1}$, $B' = 10^{-10} \ \text{cm}^3 \ \text{s}^{-1}$, $A_{nr} = 2 \times 10^8 \ \text{s}^{-1}$, $C = 10^{-29} \ \text{cm}^6 \ \text{s}^{-1}$, $n_0 = 10^{18} \ \text{cm}^{-3}$, $\alpha_i = 10 \ \text{cm}^{-1}$, $n_r = 4$, $r = 0.999$, $\beta = 10^{-1}$. Parameters for (e) and (f): $V = (0.1 \ \mu\text{m} \times 0.1 \ \mu\text{m} \times 10 \ \text{nm})$, $\Gamma = 0.25$, $a = 2.5 \times 10^{-18} \ \text{cm}^2 \ \text{s}^{-1}$, $B' = 10^{-10} \ \text{cm}^3 \ \text{s}^{-1}$, $n_0 = 10^{18} \ \text{cm}^{-3}$, $\alpha_i = 1 \ \text{cm}^{-1}$, $n_r = 4$, $r = 1 - 10^{-6}$, $\beta = 10^{-4}$.

state characteristics for lasers with different active volumes. Continuum mean-field rate-equation results are compared with those obtained from the biased random walk technique. All the devices considered operate in the limit where strong coherent effects, such as Rabi oscillations, are absent [4,24].

Figures 4(a) and 4(b) show results for a Fabry-Perot laser diode with $\beta = 5 \times 10^{-5}$ and active volume $V = 33.6 \ \mu\text{m}^3$. The expected classical laser threshold behavior and carrier pinning above threshold is observed. Total optical output power in mW at an operating emission wavelength of 1310 nm can be determined by multiplying the photon number by 5.2×10^{-5}.

Figures 4(c) and 4(d) give results for a microdisk laser with active volume $V = 0.12 \ \mu\text{m}^3$. Optical output power in μW at 1310-nm wavelength is obtained by multiplying the photon number by 7.1×10^{-3}. The steady-state characteristics show that the change in slope of $\langle s \rangle$ around the phase transition region is considerably smoothed due to the large value of $\beta = 0.1$.
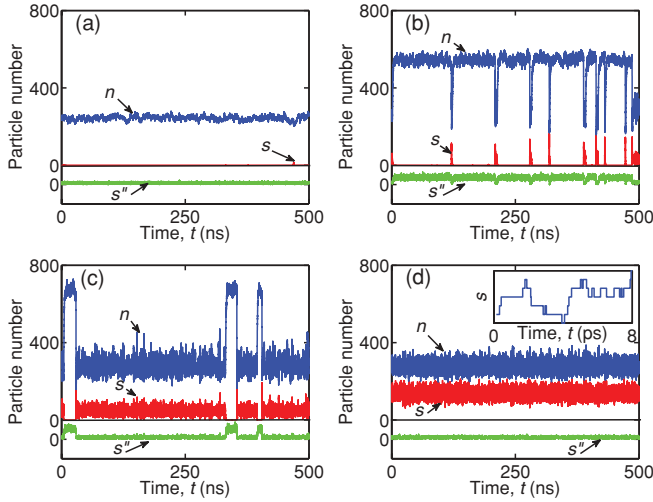
FIG. 5. (Color online) Time evolution of electrons and photons calculated by a random trajectory. (a) Current, $I = 9.6$ nA, (b) $I = 48$ nA, (c) $I = 72$ nA, (d) $I = 192$ nA. The inset shows discrete step changes in photon number with time. Parameters are as in Figs. 4(e) and 4(f): $V = (0.1 \ \mu\text{m} \times 0.1 \ \mu\text{m} \times 10 \ \text{nm})$, $\Gamma = 0.25$, $a = 2.5 \times 10^{-18}$ cm^2 s^{-1}, $B' = 10^{-10}$ cm^3 s^{-1}, $n_0 = 10^{18}$ cm^{-3}, $\alpha_i = 1$ cm^{-1}, $n_r = 4$, $r = 1 - 10^{-6}$, $\beta = 10^{-4}$.

Figures 4(e) and 4(f) give the steady-state characteristics of a laser where the active volume has been reduced to $V = 10^{-4} \ \mu\text{m}^3$ and $\beta = 10^{-4}$. Suppression of lasing is observed along with depinning of carriers in the limit of small active volume and small β values. Optical output power in nW at a wavelength of 800 nm is obtained by multiplying the photon number by 0.186.

Carrier depinning near threshold may be investigated further by accounting for spontaneous emission of photons into a nonlasing channel. The $(1 - \beta)$ term (Fig. 3) populates another channel containing s'' photons which decay at the same rate as the cavity photons. This channel does not participate in any stimulated photon processes.

Figure 5 shows trajectories calculated in the time domain for different injection currents for a very small active volume laser with parameters as in Figs. 4(e) and 4(f). The spontaneous emission terms are also included in the calculation. The calculated time-domain data in Figs. 5(a) and 5(b) show bursts of photons because of the presence of large fluctuations and the injection current is not great enough to sustain continuous lasing. With increasing injection current, longer lasting photon bursts result in a double-peaked average electron distribution. This is well illustrated by the data in Fig. 5(c). For operation near threshold switching occurs between two different characteristic system states. Figure 5(d) is an example of strong lasing with quantized photon fluctuations about a mean value $\langle s \rangle = 136$. This trajectory compares closely to the Langevin trajectories generated by adding Gaussian noise to the continuum mean-field rate equations. This analogy is considered in greater detail in Sec. IV B. The average output power from both cavity mirrors is around 25 nW at an operating wavelength of 0.8 μm. In this case $s'' = 9.5$.

There is less noise in carrier number n in Fig. 5(a) when there are essentially only electrons in the system and very few lasing photons. As illustrated in Fig. 5(c), when both photons

and electrons are in the system the electron noise is enhanced because photon noise couples into the electron distribution. When the cavity empties of photons, the number of electrons increases but the noise decreases. This is because noise coupled into the electron system from the photons is no longer present.

The Fano factor, F, may be used to quantify photon fluctuations:

$$F = \sigma_s^{\ 2} / \langle s \rangle, \qquad (3)$$

where σ_s is the standard deviation in photon number. The phase transition in a conventional laser is accompanied by large photon fluctuations and this quantity peaks sharply across lasing threshold, I_{th}. For large injection currents, $I \gg I_{\text{th}}$, the Fano factor approaches unity, corresponding to a Poisson distribution. For small active volumes the sharp transition is replaced by a broad peak in the Fano factor in the vicinity of the threshold, and $F > 1$, indicating a non-Poisson distribution.

In Fig. 6 the steady-state laser characteristics of (i) a large active volume device ($V = 5 \ \mu\text{m}^3$), (ii) an intermediate volume ($V = 5 \times 10^{-3} \ \mu\text{m}^3$), and (iii) a small volume ($V = 10^{-4} \ \mu\text{m}^3$) are shown. The data are normalized to the large
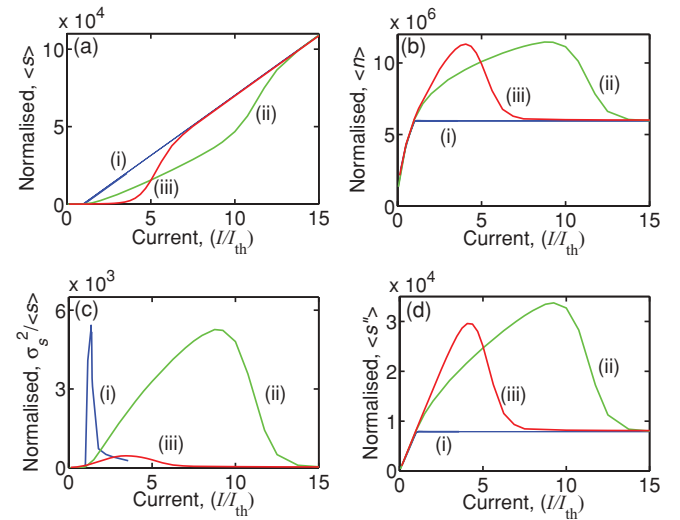

FIG. 6. (Color online) Comparison of steady-state laser characteristics for three different active volumes. (a) Normalized mean photon number versus current. (b) Normalized mean electron number versus current. (c) Normalized Fano factor versus current. (d) Normalized spontaneous emission photon number versus current. (i) Results for a large active volume, (ii) an intermediate-size active volume, (iii) a small active volume (Fig. 5). The calculations for the large active volume device matches the continuum mean-field rate-equation data closely. The current values are normalized by dividing by the respective threshold currents predicted by continuum mean-field rate equations ($I_{\text{th}-\text{i}} = 112 \ \mu\text{A}$, $I_{\text{th}-\text{ii}} = 320$ nA, $I_{\text{th}-\text{iii}} = 12.8$ nA). Normalization constants, N are: mean photon number, $\text{N}s_\text{i} = 1$, $\text{N}s_\text{ii} = 350$, $\text{N}s_\text{iii} = 800$; mean electron number, $\text{N}n_\text{i} = 1$, $\text{N}n_\text{ii} = 607$, $\text{N}n_\text{iii} = 21594$. Mean spontaneous emission photon number, $\text{N}s''_\text{i} = 1$, $\text{N}s''_\text{ii} = 370$, $\text{N}s''_\text{iii} = 855$. Fano factor, $\text{N}F_\text{i} = 1$, $\text{N}F_\text{ii} = 1$, $\text{N}F_\text{iii} = 10$. Parameters: $V_\text{i} = (5 \times 1 \times 1 \ \mu\text{m})$, $V_\text{ii} = (5 \ \mu\text{m} \times 0.1 \ \mu\text{m} \times 10 \ \text{nm})$, $V_\text{iii} = (0.1 \ \mu\text{m} \times 0.1 \ \mu\text{m} \times 10 \ \text{nm})$, $\Gamma_{\text{i,iii}} = 0.25$, $\Gamma_\text{ii} = 0.05$, $a_{\text{i,ii}} = 2.5 \times 10^{-16}$ cm^2 s^{-1}, $a_\text{iii} = 2.5 \times 10^{-18}$ cm^2 s^{-1}, $B' = 10^{-10}$ cm^3 s^{-1}, $n_0 = 10^{18}$ cm^{-3}, $\alpha_i = 10$ cm^{-1} for (i,ii), $\alpha_i = 1$ cm^{-1} for (iii), $n_r = 4$, $r_{\text{i,ii}} = 0.999$, $r_\text{iii} = 1 - 10^{-6}$, and $\beta = 10^{-4}$.

active volume device continuum mean-field rate-equation predictions for $\langle n \rangle$ and $\langle s \rangle$. Figure 6(a) compares $\langle s \rangle$ as a function of I between different cavities and convergence with the continuum mean-field rate equations is achieved for the largest cavity. Lasing is increasingly suppressed with the reduction of active volume. The normalized Fano factor as a function of normalized current exhibits a peak around the threshold region. As expected, the largest active volume device exhibits the sharpest threshold behavior. In general, the peak identifies the presence of strong fluctuations and non-Poisson photon statistics around threshold. Carrier depinning accompanies photon fluctuations, as demonstrated by Fig. 6(b). Figure 6(d) shows enhanced spontaneous emission across threshold resulting from the extra carriers contributed by carrier depinning. An explanation of lasing suppression, enhanced spontaneous emission and depinning of carriers may be found in the time-domain data illustrated in Fig. 5(c). The system fails to lase continuously in this region and switches between the lasing and nonlasing state. Once the system shuts down, it waits for the next spontaneous emission event to reinitiate lasing. Lasing, being predominantly a stimulated process, requires the presence of photons in the cavity. A larger active volume with a larger number of electrons has more spontaneous emission events, which prevents lasing shutdown. A smaller active volume, with lesser likelihood of such events, experiences suppression of continuous lasing. Lasing shutdown is accompanied by depinning of carriers, which in turn enhances spontaneous emission.

III. MASTER EQUATIONS

The predictions of the biased random walk technique can be verified independently by use of coupled deterministic differential equations that quantize particle number. Previously, such master equations have been solved to explore steady-state behavior in the limit of cavity quantum electrodynamics for which $\beta = 1$ [25,26]. Biased random walk trajectories in (n, s) space can be used to sample solutions of master equations.

The equation describing time evolution of probability $P_{n,s}$ of states (n, s) in a single-mode semiconductor laser diode with photon emission at energy $\hbar\omega$ is of the form

$$
\begin{aligned}
\frac{dP_{n,s}}{dt} = {} & -\kappa[sP_{n,s} - (s+1)P_{n,s+1}] - [sG_n P_{n,s} \\
& - (s-1)G_{n+1}P_{n+1,s-1}] - [sAP_{n,s} \\
& - (s+1)AP_{n-1,s+1}] - \beta B[n^2 P_{n,s} \\
& - (n+1)^2 P_{n+1,s-1}] - (1-\beta)B[n^2 P_{n,s} \\
& - (n+1)^2 P_{n+1,s}] - \frac{I}{e}(P_{n,s} - P_{n-1,s}), \quad (4)
\end{aligned}
$$

where the active volume is V and the device is driven by current I. The term $-\beta Bn^2 P_{n,s}(t)$ describes spontaneous emission of photons involving transitions from state (n, s) to state $(n-1, s+1)$, where $B = B'/V$ and B' is the spontaneous emission coefficient. $-sG_n P_{n,s}(t)$ describes stimulated emission of photons from state (n, s) to state $(n-1, s+1)$, where G_n is the stimulated emission coefficient. $-(1-\beta)Bn^2 P_{n,s}(t)$ is the decay of electrons into nonlasing photons via transitions from state (n, s) to state $(n-1, s)$. $-IP_{n,s}(t)$ corresponds

to injection of electrons causing transitions from state (n, s) to state $(n+1, s)$. $-AsP_{n,s}(t)$ is stimulated absorption of photons involving transitions from state (n, s) to state $(n+1, s-1)$, where A is the stimulated absorption coefficient. $-\kappa sP_{n,s}(t)$ describes the decay of cavity photons in which transitions from state (n, s) to state $(n, s-1)$ occur, where κ is the optical loss coefficient.

The time evolution of $P_{n,s}$ can be solved by integrating (4). $P_{n,s}$ may also be solved under steady-state conditions by truncating the system at values of n and s which are much larger than the steady-state mean values predicted by the continuum mean-field rate equations [25–27]. The equations governing the mean behavior are derived by averaging the master equations over all possible states, after multiplying by n and s. This gives

$$
\frac{d\langle n \rangle}{dt} = -B\langle n^2 \rangle - \frac{a\Gamma c}{Vn_r}\langle (n - n_0)s \rangle + \frac{I}{e}, \quad (5)
$$

$$
\frac{d\langle s \rangle}{dt} = \beta B\langle n^2 \rangle + \frac{a\Gamma c}{Vn_r}\langle (n - n_0)s \rangle - \kappa\langle s \rangle, \quad (6)
$$

which reduces to the standard continuum mean-field rate equations if the correlations factorize such that $\langle (n - n_0)s \rangle = \langle (n - n_0) \rangle \langle s \rangle$ and $\langle n^2 \rangle = \langle n \rangle^2$. The second approximation is valid in the case of narrow, symmetric single-peaked distributions in n. A system involving a small number of particles experiences strong fluctuations in particle number and correlations between n and s are significant. Hence, such mean-field approximations are not valid, leading to predictions of mean behavior that are different from a more complete probabilistic picture.

Figure 7 illustrates some of the essential differences by showing the results of calculating the steady-state characteristics with master equations (M.E.) and continuum mean-field rate equations (R.E.). The $\langle ns \rangle$ correlation differs most from its factorized product $\langle n \rangle \langle s \rangle$ around threshold [Fig. 7(d)] and the master equations accounting for these correlations differ significantly in its predictions. In particular, it leads to suppression of lasing by increasing the apparent threshold current [Fig. 7(a)] and depinning of carriers [Fig. 7(b)]. Assuming the value of current at the Fano-factor peak may be used as a measure of laser threshold [24], Fig. 7(c) gives a threshold $I_{\text{th}} = 45$ nA, which is 4.5 times greater than the value of $I_{\text{th}} = 10$ nA predicted by continuum mean-field rate equations. The differences reduce as one scales to a larger number of particles in the limit of conventional laser operation and this was indeed verified by master-equation calculations performed for a system with parameters similar to those in Fig. 7 but with a higher value of β. Figures 7(e) and 7(f) show the probability distribution of photons P_s and electrons P_n for different stages of laser operation. At low injection currents, P_s is bimodal with a large probability for occupation of the photon ground state, $s = 0$. This indicates that quantum fluctuations cause lasing emission to turn off. The probability distribution for P_s and P_n near I_{th} is bimodal, confirming the existence of the two characteristic system states. Only when $I \gg I_{\text{th}}$ do P_s and P_n become single peaked. The probability distribution for these injection currents obtained from the master equations are in agreement with results of the trajectory method shown in Fig. 5. In the long-time limit, trajectories in the (n, s) plane are
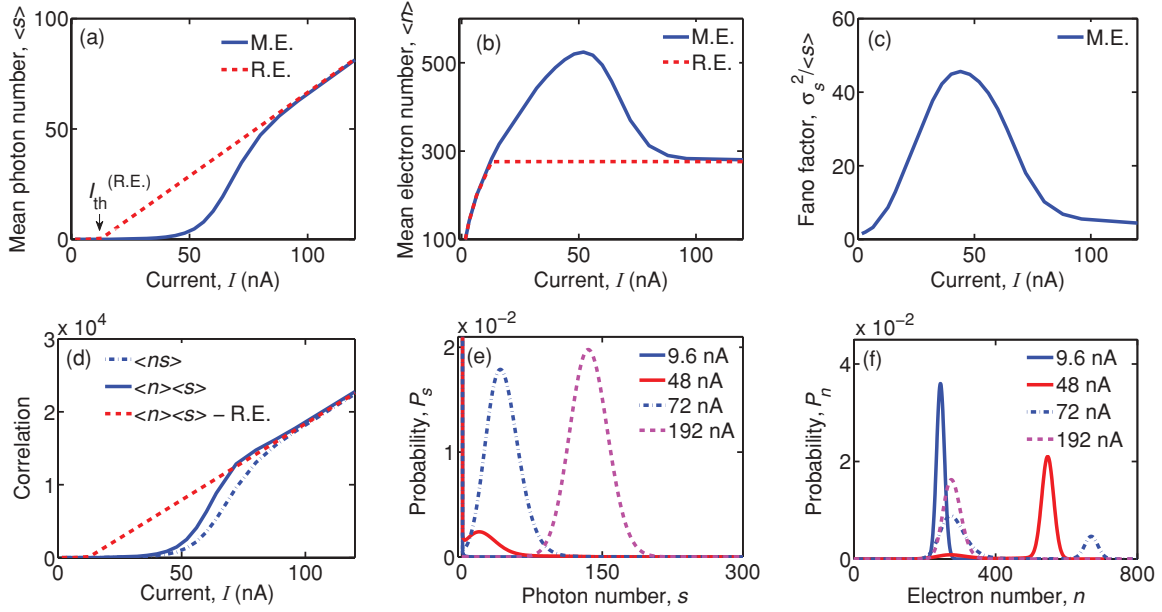
FIG. 7. (Color online) Steady-state characteristics. (a) Calculated mean photon number as a function of current showing that master equations (M.E.) predict suppression of lasing threshold relative to continuum mean-field rate-equation (R.E.) calculations. Suppression in lasing is due to quantum fluctuations. (b) Calculated mean electron number as a function of current. M.E. show carrier depinning due to quantum fluctuations. (c) Fano factor $F = \sigma_s^2/\langle s \rangle$ as a function of current, I. (d) Electron-photon correlation and product of means versus current. (e) Probability of photons for different currents. (f) Probability of electrons for different currents. Parameters are as in Fig. 5. Figures are from [23].

found to converge to the predictions of the master equations (Fig. 8).

Computational convenience dictates the choice of parameters used for solving the master equations. Realistic parameters increase number of particles, which in turn leads to a large number of probability states. For total number of particles N, the number of probability states is $D = (N + 1)(N + 2)/2$ and this grows as N^2 for large N. For $N = 1000$ the probability vector has a length of 0.5×10^6. Matrix inversion for steady-state calculation and multiplication for time evolution becomes difficult when the size of the coefficient matrix (D^2) increases significantly beyond this value.

Despite the use of small values of n and s, the underlying physics in which quantum fluctuations suppress lasing and carriers are depinned remain. This is confirmed by calculations using the trajectory method which was developed to connect with large systems described by realistic parameters. The technique verifies master-equation results and predicts similar behavior in small systems with experimentally accessible parameters (see Sec. V).

Similar to the trajectory method, the master equations can be modified to include spontaneous emission of photons into a nonlasing channel. The spontaneous emission channel does not participate in any stimulated processes and so avoids the correlation effects that strongly influence lasing emission. The master equation for probability $P_{n,s,s''}(t)$ is (4), with additional terms $(1 - \beta)Bn^2 P_{n,s,s''}$ corresponding to decay of electrons into photons of the nonlasing channel, causing a transition from state (n, s, s'') to $(n - 1, s, s'' + 1)$, and $\kappa s'' P_{n,s,s''}$ denoting decay of nonlasing photons, causing a transition from state (n, s, s'') to $(n, s, s'' - 1)$. The average value for n and s obtained using $P_{n,s,s''}(t)$ gives Eqs. (5) and (6), respectively.

The average for s'' is

$$\frac{d\langle s'' \rangle}{dt} = (1 - \beta)B\langle n^2 \rangle - \kappa \langle s'' \rangle. \tag{7}$$

Large fluctuations and correlations in particle number in the finite-sized quantum system lead to carrier depinning near threshold and the increased average number of carriers results in enhanced spontaneous emission because of the $(1 - \beta)Bn^2$ dependence. This is verified by the trajectory method [Fig. 6(d)]. A similar plot using master-equation calculations is avoided for numerical reasons. The system has a larger number of probability states due to the presence of this additional channel of spontaneously emitted photons. However, a similar idea may be demonstrated by studying the role of β in distributing the total emission between two modes. Larger β enhances spontaneous emission into the lasing mode and prevents lasing shutdown. Reducing β has the opposite effect. Figure 8 demonstrates this for a small active volume. As β is reduced, while keeping the current constant, the emission switches from being dominated by lasing to being dominated by spontaneous emission. This leads to lasing suppression. The peak at higher electron number in the bimodal distribution corresponding to zero lasing photons gives rise to enhanced spontaneous emission. The distribution of spontaneous emission as shown in Figs. 8(c) and 8(d) is symmetric in the absence of diagonal processes illustrated in the state diagram shown in Fig. 3. The active volumes used for calculations whose results shown in Figs. 8(a)–8(d) are chosen for computational convenience. The same calculations have been repeated using the trajectory method for a larger system and a similar behavior is observed with change of β.
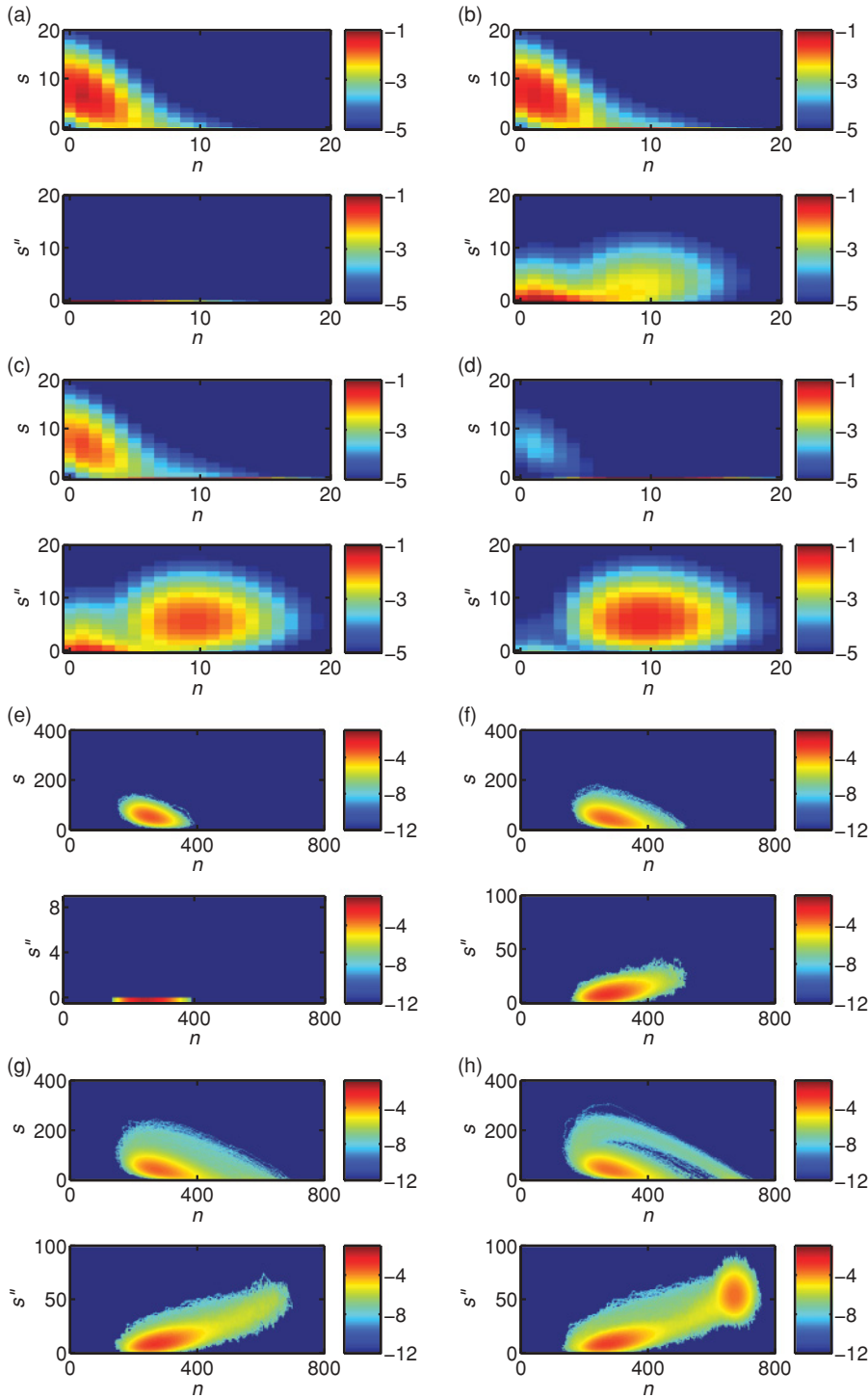
FIG. 8. (Color online) Steady-state probability distribution for electrons (n), photons (s), and spontaneous emission (s'') for different values of β and a fixed current $I = 10$ electron/ns ($=1.6$ nA) for (a), (b), (c), and (d) and 72 nA for (e), (f), (g), and (h). (a) and (e) $\beta = 1$, (b) and (f) $\beta = 10^{-1}$, (c) and (g) $\beta = 10^{-2}$, (d) and (h) $\beta = 10^{-4}$. Parameters for (a), (b), (c), and (d) are as in Fig. 5 but with $V = (1 \ \mu\text{m} \times 1 \ \text{nm} \times 1 \ \text{nm})$ and $\alpha_i = 0.19 \ \text{cm}^{-1}$. Parameters for (e), (f), (g), and (h) are as in Fig. 5. The color (gray) scale is $\log_{10}$.

IV. TRANSIENT DYNAMICS IN SMALL LASERS

To solve the transient master equation, the entire time evolution is divided into equal time intervals, the duration of which is determined by the inverse of the pumping rate. This allows only a single electron to enter the active volume on average in a given time interval. If we start with an empty device [i.e., $P_{0,0}(t = 0) = 1$], the terms which will be important in the first time interval are $P_{0,0}$, $P_{0,1}$, $P_{1,0}$. This happens because a system of n electrons and s photons can only undergo processes and make single quantum transitions as described in Fig. 3. We integrate the set of master equations involving these terms using the fourth-order Runge-Kutta method for the first interval. In the next interval the maximum number of particles is 2. So terms such as $P_{1,1}$, $P_{0,2}$, $P_{2,0}$ will be important along with the terms of the previous interval. With the addition of the nth electron, $n + 1$ additional probability states are added and the coefficient matrix grows as D^2. For a given interval the process is similar to a continuous-time Markov process where the allowed states are the states of the continuous-time Markov chains. The system of equations
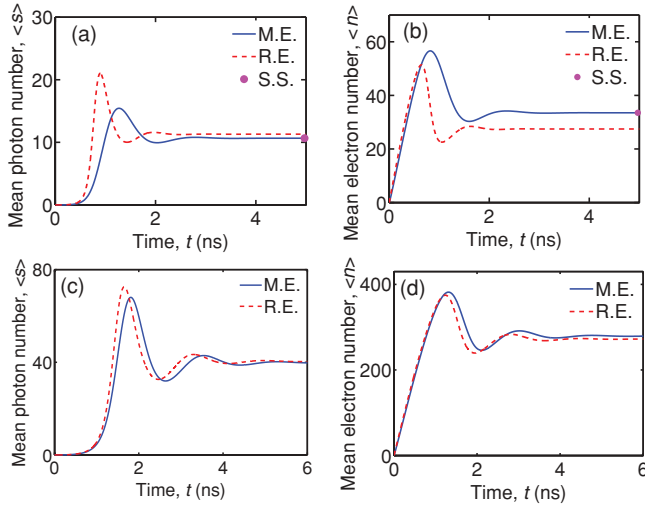
FIG. 9. (Color online) Transient behavior of mean electron number and photon number for a step change in current from $I(t < 0) = 0$ to $I(t \geqslant 0) = 100$ electrons/ns (16 nA) for (a) and (b) and $I(t \geqslant 0) = 400$ electrons/ns (=64 nA) for (c) and (d). (a) Mean photon number as a function of time. (b) Mean electron number as a function of time. The dot at the last time point denotes the mean calculated from the probability distribution obtained by the steady-state technique. Parameters as in Fig. 5 but with $V = (0.1 \, \mu\text{m} \times 10 \, \text{nm} \times 10 \, \text{nm})$ and $\beta = 10^{-1}$. (c) Mean photon number as a function of time. (d) Mean electron number as a function of time. Parameters as in Fig. 5 but with $\beta = 10^{-1}$. Panels (a) and (b) are from [23].

is such that total probability is conserved in every step as more electrons enter the system. Iterations are continued by adding more particles until the system attains a steady-state probability distribution. The steady state attained agrees with the one obtained from the truncated master equations solved under steady-state conditions.

Figures 9(a) and 9(b) show the time evolution of $\langle n \rangle$ and $\langle s \rangle$ for a small laser operating above threshold. Factorization of the correlation $\langle ns \rangle$ is not appropriate, as reflected by the fact that the continuum mean-field rate-equation results do not converge to the master-equations solution. Figures 10(b) and 10(c) show that at any point in time the instantaneous probability $P_{n,s}$ carries information about the path taken. In

contrast, averaging in the continuum mean-field rate-equation calculation removes information about the system's history.

Strong correlations and fluctuations affect the average response of a small laser to a step change in injection current and slows down the system in general. Increasing the active volume, keeping other parameters fixed, reduces the difference with the mean-field predictions [Figs. 9(c) and 9(d)].

A. Large-signal analysis

A large-signal analysis may be performed by starting from the system ground state and observing the response to a step change in injection current. The time delay, t_d, may be calculated by starting from an empty device ($n, s = 0$) and noting the time taken to reach half the steady-state photon number. The mean time, $\langle t_d \rangle^{\text{MC}}$, calculated by averaging t_d for multiple trajectories obtained using the trajectory method, is found to be in close agreement with that predicted by master equations. This is denoted by the dot in Fig. 11(a), which shows the agreement and a mean time delay $\langle t_d \rangle^{\text{MC}}$ that is greater than the predictions of the continuum mean-field rate-equation theories, $\langle t_d \rangle^{\text{RE}}$. These calculations are carried out for injection currents which support continuous lasing and hence are far away from the fluctuation dominated regime [Fig. 5(c)]. The peak of the Fano factor for the lasers considered in Figs. 11(b), 11(c), and 11(d) occur around 0.6, 8, and 150 μA, respectively, and injection current chosen for this analysis is higher than that. The Fano-factor peak gives an estimate of the threshold for these small devices [24]. Figures 11(b), 11(c), and 11(d) show a comparison of time delay for three different active volumes and convergence with continuum mean-field rate equations is achieved for the largest volume [Fig. 11(d)]. The deviation from the mean-field calculations reduces with increase in active volume size.

B. Small-signal analysis

Above threshold the biased random walk trajectory in the time domain [Fig. 5(d)] appears similar to the trajectories produced by Langevin equations as described in [28]. The Fourier transform of this data is computed to obtain small-signal relative intensity noise (RIN) data. Such time-domain analysis is not possible using master equations.
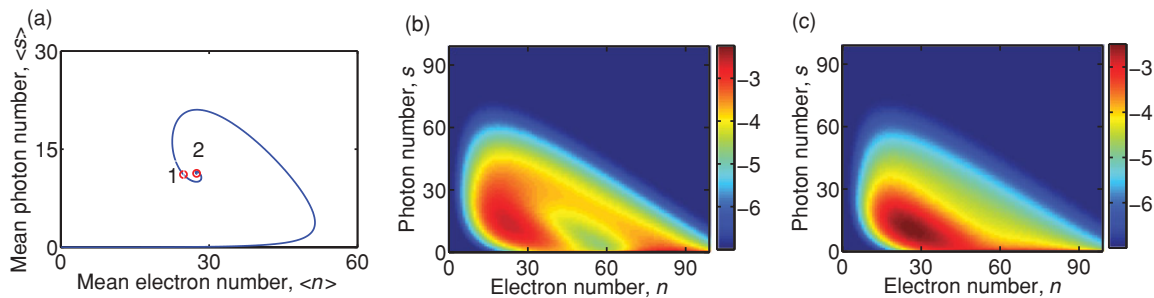

FIG. 10. (Color online) Transient behavior of mean electron number and photon number for a step change in current from $I(t < 0) = 0$ to $I(t \geqslant 0) = 100$ electrons/ns (=16 nA). (a) Evolution of mean photon number as a function of mean electron number, calculated from continuum mean-field rate equations. (b) $P_{n,s}$ calculated at time $t = 1.25$ ns and indicated by circle labeled 1 in (a). (c) $P_{n,s}$ calculated at time $t = 5$ ns and indicated by circle labeled 2 in (a). Parameters are as in Fig. 5 but with $V = (0.1 \, \mu\text{m} \times 10 \, \text{nm} \times 10 \, \text{nm})$ and $\beta = 10^{-1}$. The color (gray) scale is $\log_{10}$. Panels (b) and (c) are from [23].
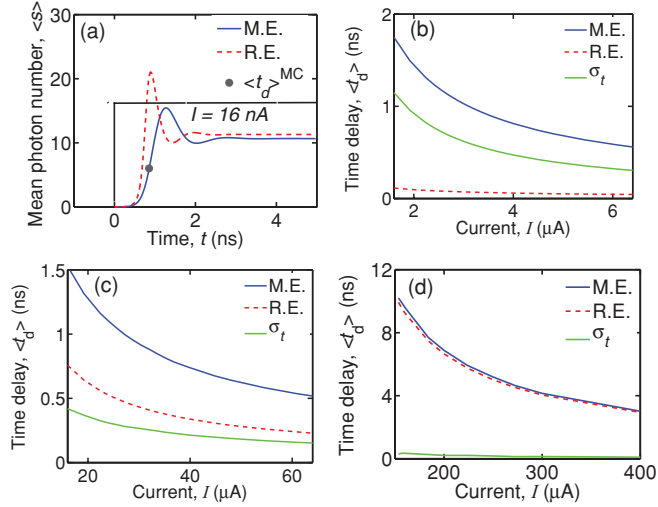
FIG. 11. (Color online) Comparison of time delay, t_d, between continuum mean-field rate equations and random walk approach. (a) Transient behavior of mean photon number for a step change in current from $I(t < 0) = 0$ A to $I(t \geqslant 0) = 16$ nA. Time delay $\langle t_d \rangle$ comparison for (b) $V = 5 \times 10^{-4} \ \mu m^3$, (c) $V = 5 \times 10^{-2} \ \mu m^3$, and (d) $V = 5 \ \mu m^3$. Parameters: (a) $V = (0.1 \ \mu m \times 10 \ nm \times 10 \ nm)$, $\Gamma = 0.25$, $a = 2.5 \times 10^{-18} \ cm^2 \ s^{-1}$, $B' = 10^{-10} \ cm^3 \ s^{-1}$, $n_0 = 10^{18} \ cm^{-3}$, $\alpha_i = 1 \ cm^{-1}$, $n_r = 4$, $r = 1 - 10^{-6}$, $\beta = 10^{-1}$. (b) $V = (5 \times 0.01 \times 0.01 \ \mu m)$, $\Gamma = 0.25$, $a = 2.5 \times 10^{-16} \ cm^2 \ s^{-1}$, $B' = 10^{-10} \ cm^3 \ s^{-1}$, $n_0 = 10^{18} \ cm^{-3}$, $\alpha_i = 10 \ cm^{-1}$, $n_r = 4$, $r = 0.999$, $\beta = 10^{-4}$. (c) $V = (5 \times 0.1 \times 0.1 \ \mu m)$; other parameters same as in (b). (d) $V = (5 \times 1 \times 1 \ \mu m)$; other parameters are as in (b).

Figures 12(a) and 12(b) show the time trajectories calculated using our trajectory method and Langevin equations, respectively. The fluctuations in photon number are noticeably larger in Fig. 12(a) than in Fig. 12(b). Our trajectory calculations show larger fluctuations and hence larger Fano factors and this trend is observed in smaller active volume lasers as well.

The Langevin equations consider correlated noise terms which are artificially forced to be Gaussian in nature. This gives rise to considerably lower values of Fano factor in the threshold region. The Langevin approach arbitrarily assumes near Poisson distributions which is physically unrealistic in the correlated system we consider. The distributions obtained from the trajectory technique are not biased to be Gaussian and

are, in fact, super-Poissonian with a much larger Fano factor even when the system is lasing continuously. For example, for a current of 400 μA, which is 2.7 times threshold current, Langevin equations give a Fano factor of about 12 and our trajectory method gives a Fano factor of near 270.

The response in the frequency domain was compared with the RIN data obtained from Langevin equations with cross-correlated noise sources [28]. The frequency response calculated using the two models agrees around the RIN peak and when the system is in the lasing state [Fig. 12(c)]. The peak in frequency increases with electron injection current. There are, however, differences at frequencies below the RIN peak. These can be brought into closer agreement by increasing the magnitude of the Langevin noise terms.

V. EXPERIMENTAL DESIGN

The behavior of lasers with very small active volumes can be studied using semiconductor nanowire [29], quantum pillar [30], or other geometries [31,32]. The active medium may be confined inside a high-Q photonic crystal or other optical cavity. Reducing the size of the laser is generally accompanied by an increase in β. However, small β is an important factor leading to lasing suppression and might explain why suppression of lasing by quantum fluctuations has not been observed in experiments.

We have performed calculations to find experimentally accessible conditions where the impact of quantum fluctuations on laser performance may be observed. Figures 13(a) and 13(b) show calculations for a system of three nanowires confined in a photonic crystal medium. Parameters chosen are similar to those considered by [29]. The lasing suppression is seen to disappear with the increase in β. The carrier depinning effect, however, persists longer and can be observed in spontaneous emission. So one of the key directions for design is to have strong confinement for the single lasing mode along with significant emission into the nonlasing modes. For a nanowire system this would mean strong confinement in the axial direction for the laser mode with spontaneous emission in the lateral directions. Reduction in β by increasing the optical cavity length is also considered in Figs. 13(c) and 13(d). Other than an overall change in the threshold value, these laser designs show a similar trend with change of β.
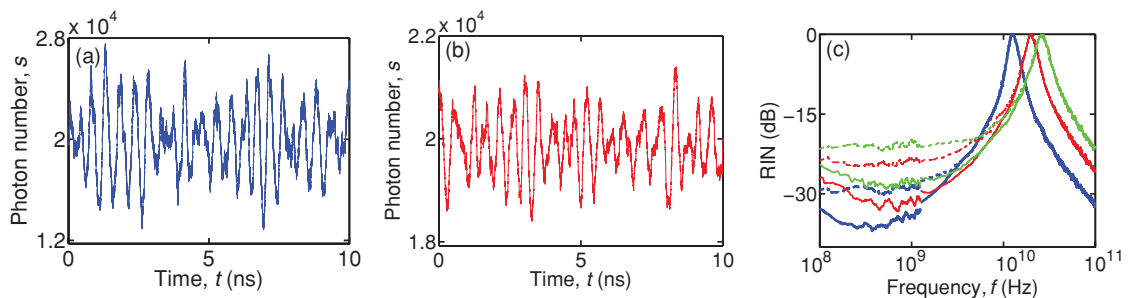

FIG. 12. (Color online) (a) Time trajectory calculated using the random walk technique. (b) Time trajectory from the Langevin equations using correlated noise sources. (c) Relative intensity noise (RIN) as a function of frequency. Calculation using Langevin equations (dashed lines), random walk calculation (solid lines). Calculations are normalized to peak in spectrum. Electron injection current = 400 μA (dark curve), 800 μA (gray curve), 1.32 mA (light gray curve). Parameters are as in Fig. 11(d).
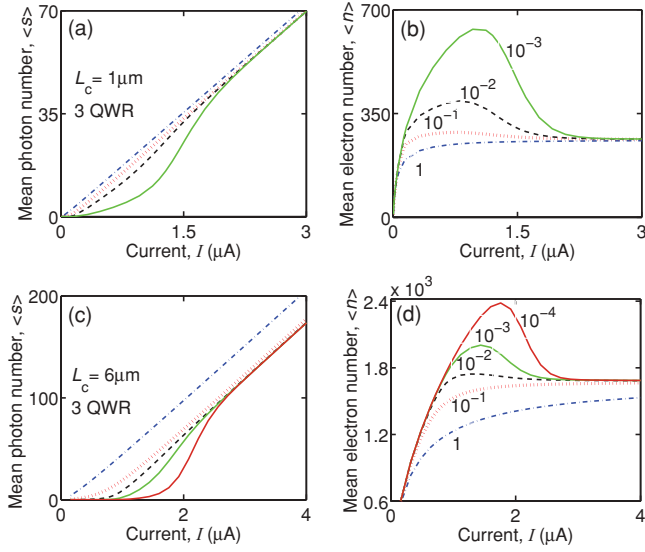
FIG. 13. (Color online) Comparison of steady-state characteristics for different β values. $\beta = 10^{-3}$ (solid), $\beta = 10^{-2}$ (dashed), $\beta = 10^{-1}$ (dot), $\beta = 1$ (dash-dot). $\beta = 10^{-4}$ (solid, dark line) is included in (c) and (d) for a larger size cavity. The graphs display random trajectory calculations. Parameters for (a) and (b): $V = 3 \times (1 \ \mu\text{m} \ \times 5 \ \text{nm} \ \times 5 \ \text{nm})$, $\Gamma = 0.01$, $a = 12.3 \times 10^{-16} \ \text{cm}^2 \ \text{s}^{-1}$, $B' = 5.5 \times 10^{-10} \ \text{cm}^3 \ \text{s}^{-1}$, $A_{\text{nr}} = 0.91 \times 10^9 \ \text{s}^{-1}$, $C = 0.5 \times 10^{-29} \ \text{cm}^6 \ \text{s}^{-1}$, $n_0 = 10^{18} \ \text{cm}^{-3}$, $\alpha_i = 0.0010 \ \text{cm}^{-1}$, $n_r = 3.5$, $r = 0.997$, $\epsilon = 0.01 \times 10^{-18} \ \text{cm}^3$. Parameters for (c) and (d): $V = 3 \times (6 \ \mu\text{m} \ \times 5 \ \text{nm} \ \times 5 \ \text{nm})$, $\Gamma = 0.004$, $\alpha_i = 5 \ \text{cm}^{-1}$, $r = 0.995$; others are as in (a) and (b). Net optical output power in μW at an operating wavelength of 1310 nm may be determined by multiplying the photon number by 0.039 for (a) and (b) and 0.0109 for (c) and (d).
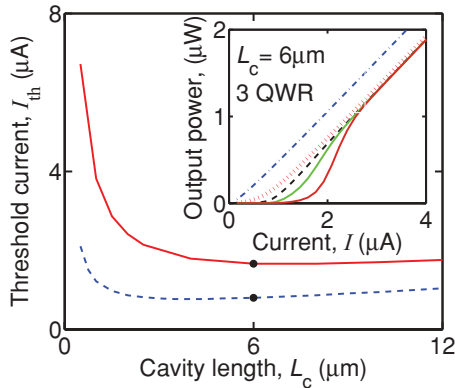

FIG. 14. (Color online) Variation of threshold current with cavity length. The upper curve (solid) represents results of random trajectory calculations and the lower curve (dashed) represents results of continuum mean-field rate-equation calculations. $\beta = 10^{-4}$ for main figure. The inset is a comparison of steady-state characteristics for different β values. $\beta = 10^{-4}$ (solid, dark line), $\beta = 10^{-3}$ (solid), $\beta = 10^{-2}$ (dashed), $\beta = 10^{-1}$ (dotted), $\beta = 1$ (dash-dotted). This is the same plot as in Fig. 13(c) but in terms of output power for an operating wavelength of 1310 nm. Parameters are as in Fig. 13(c).
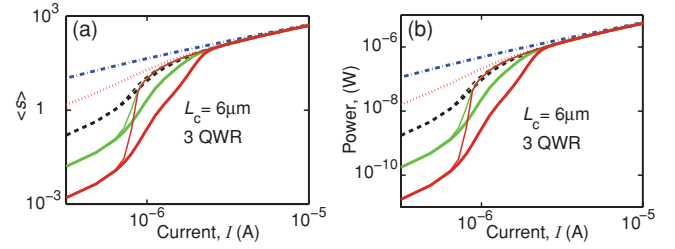

FIG. 15. (Color online) Comparison of steady-state characteristics for different β values. $\beta = 10^{-4}$ (solid, dark line), $\beta = 10^{-3}$ (solid), $\beta = 10^{-2}$ (dashed), $\beta = 10^{-1}$ (dotted), $\beta = 1$ (dash-dotted). Thicker lines are results of random walk calculation; thinner lines are from the continuum mean-field calculations. (a) Intracavity mean photon number, (b) output optical power versus injection current. Parameters are as in Figs. 13(c) and 13(d).

The threshold current, I_{th}, for the laser considered in Figs. 13(c) and 13(d) is shown in Fig. 14 as a function of cavity length, L_c. In this case, changing the cavity length alters the active volume. The rate-equation data are compared with the random walk trajectory calculation. Only the case with $\beta = 10^{-4}$ is considered. The peak of the Fano factor is used to locate the threshold current in the random trajectory calculations. Threshold current is larger than the predictions of continuum mean-field rate equations due to lasing suppression. The light output characteristics of the laser with $L_c = 6 \ \mu$m is considered in the inset. This has a threshold current around $2 \ \mu$A and optical output power is in the μW range. As expected, the pinned carrier number has a linear dependence on the cavity length, L_c.

Figure 15 is a plot of steady-state characteristics using a $\log_{10}$ scale. These correspond to the linear plot of Fig. 13(c). Strong quantum fluctuations around threshold smooth the nonlasing-to-lasing transition compared to a more abrupt crossover predicted by the continuum mean-field theories. This is seen for the small β cases where the effects of lasing suppression becomes apparent.

VI. CONCLUSION AND OUTLOOK

In conclusion, our calculations illustrate the importance of quantum fluctuations in determining the steady-state and transient responses of a laser when there are a small number of particles in the system. Quantum fluctuations can suppress lasing threshold, enhance spontaneous emission, and create a non-Poisson probability distribution for n discrete excited electronic states and s discrete photons. Correlations between n and s are found to damp the average dynamic response of laser emission. Fluctuations in the finite-sized quantum system behave differently from lasers in the thermodynamic limit. According to the conventional Landau-Ginzburg theory of phase transitions, fluctuations in the large particle number limit enhance lasing below threshold. In meso-scale systems the opposite is true; quantum fluctuations suppress lasing.

The master equations and the random walk technique generate statistics of the photon field but do not include phase as they only quantize energy. Phase fluctuation carries information about linewidth of the lasing mode. Inclusion

of phase in a fully quantum mechanical model solved by brute-force methods is challenging due to the extremely large state space for the system. A possible approach might be to solve for a few atoms in the optical cavity and then attempt to develop techniques capable of solving the problem for larger numbers of particles based on the physical insight gained.

[1] H. Haken, in *Handbuch der Physik*, edited by L. Genzel (Springer, Berlin, 1970), Vol. XXV/2c.

[2] M. O. Scully and W. E. Lamb, Phys. Rev. Lett. **16**, 853 (1966).

[3] M. O. Scully and W. E. Lamb, Phys. Rev. **159**, 208 (1967).

[4] M. O. Scully and M. Suhail Zubairy, *Quantum Optics* (Cambridge University Press, Cambridge, UK, 1997).

[5] J. O'Gorman, A. F. J. Levi, S. Schmitt-Rink, T. Tanbun-Ek, D. L. Coblentz, and R. A. Logan, Appl. Phys. Lett. **60**, 157 (1992).

[6] J. O'Gorman, S. L. Chuang, and A. F. J. Levi, Appl. Phys. Lett. **62**, 1454 (1993).

[7] S. L. Chuang, J. O'Gorman, and A. F. J. Levi, IEEE J. Quantum Electron. **29**, 1631 (1993).

[8] S. L. McCall, A. F. J. Levi, R. E. Slusher, S. J. Pearton, and R. A. Logan, Appl. Phys. Lett. **60**, 289 (1992).

[9] G. Bjork and Y. Yamamoto, IEEE J. Quantum Electron. **27**, 2386 (1991).

[10] H. Yokoyama and S. D. Bronson, J. Appl. Phys. **66**, 4801 (1989).

[11] F. De Martini, F. Cairo, P. Mataloni, and F. Verzegnassi, Phys. Rev. A **46**, 4220 (1992).

[12] E. Purcell, Phys. Rev. **69**, 37 (1946).

[13] A. F. J. Levi, *Applied Quantum Mechanics* (Cambridge University Press, Cambridge, UK, 2003).

[14] A. F. J. Levi, S. L. McCall, S. J. Pearton, and R. A. Logan, Electron. Lett. **29**, 1666 (1993).

[15] G. W. Gardiner, *Handbook of Stochastic Methods* (Springer–Verlag, Berlin, 1983).

[16] W. H. Louisell, *Quantum Statistical Properties of Radiation* (Wiley, New York, 1973).

[17] J. I. Perea, D. Porras, and C. Tejedor, Phys. Rev. B **70**, 115304 (2004).

[18] O. Benson and Y. Yamamoto, Phys. Rev. A **59**, 4756 (1999).

[19] Y. Mu and C. M. Savage, Phys. Rev. A **46**, 5944 (1992).

[20] A. M. Smith and C. W. Gardiner, Phys. Rev. A **38**, 4073 (1988).

[21] M. Elk, Phys. Rev. A **54**, 4351 (1996).

[22] G. M. D'Ariano, N. Sterpi, and A. Zucchetti, Phys. Rev. Lett. **74**, 900 (1995).

[23] K. Roy-Choudhury, S. Haas, and A. F. J. Levi, Phys. Rev. Lett. **102**, 053902 (2009).

[24] R. Jin, D. Boggavarapu, M. Sargent, P. Meystre, H. M. Gibbs, and G. Khitrova, Phys. Rev. A **49**, 4038 (1994).

[25] P. R. Rice and H. J. Carmichael, Phys. Rev. A **50**, 4318 (1994).

[26] H. J. Carmichael, in *Lasers and Quantum Optics,* in *proceedings of the International School on Lasers and Quantum Optics, Mar del Plata, Argentina, 22–31 August 1988* (World Scientific, Singapore, 1990), p. 52.

[27] L. Florescu and S. John, Phys. Rev. E **69**, 046603 (2004).

[28] M. Ahmed, M. Yamada, and M. Saito, IEEE J. Quantum Electron. **37**, 1600 (2001).

[29] K. Atlasov, M. Calic, F. Karlsson, P. Gallo, A. Rudra, B. Dwir, and E. Kapon, Opt. Express **17**, 18178 (2009).

[30] H. Kim, M. T. Rakher, D. Bouwmeester, and P. M. Petroff, Appl. Phys. Lett. **94**, 131104 (2009).

[31] S. Reitzenstein, C. Boeckler, A. Bazhenov, A. Gorbunov, S. Muench, A. Loeffler, M. Kamp, V. D. Kulakovskii, and A. Forchel, Phys. Status Solidi B **246**, 277 (2009).

[32] S. Reitzenstein, T. Heindel, C. Kistner, A. Rahimi-Iman, C. Schneider, S. Höfling, and A. Forchel, Appl. Phys. Lett. **93**, 061104 (2008).